Scattering and transport statistics at the metal-insulator transition: A numerical study of the power-law banded random-matrix model

J. A. Méndez-Bermúdez
Instituto de Física, Benemérita Universidad Autónoma de Puebla, Apartado Postal J-48, Puebla 72570, Mexico

Victor A. Gopar
Depto de Física Teórica, Facultad de Ciencias, and Instituto de Biocomputación y Física de Sistemas Complejos (BIFI), Universidad de Zaragoza, Pedro Cerbuna 12, E-50009 Zaragoza, Spain

Imre Varga
Elméleti Fizika Tanszék, Fizikai Intézet, Budapesti Műszaki és Gazdaságtudományi Egyetem, H-1521 Budapest, Hungary and Fachbereich Physik und Wissenschaftliches Zentrum für Materialwissenschaften, Philipps Universität Marburg, D-35032 Marburg, Germany

(Received 14 January 2010; revised manuscript received 5 July 2010; published 8 September 2010)

We study numerically scattering and transport statistical properties of the one-dimensional Anderson model at the metal-insulator transition described by the power-law banded random matrix (PBRM) model at criticality. Within a scattering approach to electronic transport, we concentrate on the case of a small number of single-channel attached leads. We observe a smooth crossover from localized to delocalized behavior in the average-scattering matrix elements, the conductance probability distribution, the variance of the conductance, and the shot noise power by varying b (the effective bandwidth of the PBRM model) from small ($b \ll 1$) to large ($b > 1$) values. We contrast our results with analytic random matrix theory predictions which are expected to be recovered in the limit $b \to \infty$. We also compare our results for the PBRM model with those for the three-dimensional (3D) Anderson model at criticality, finding that the PBRM model with $b \in [0.2, 0.4]$ reproduces well the scattering and transport properties of the 3D Anderson model.

DOI: 10.1103/PhysRevB.82.125106 PACS number(s): 71.30.+h, 03.65.Nk, 73.23.−b

I. INTRODUCTION

The study of systems at the Anderson metal-insulator transition (MIT) has been a subject of intensive research activity for several decades.[1–4] In particular, much interest has been focused on the scattering properties of critical systems by analyzing the probability distribution functions of the resonance widths Γ and Wigner delay times τ_W,[5–14] as well as the transmission or dimensionless conductance T.[15–26] The distribution functions of Γ and τ_W have been shown to be related to the properties of the corresponding closed systems, i.e., the fractality of the eigenstates and the critical features of the MIT. On the other hand, at the MIT, the distribution of conductances $w(T)$ has been found to be *universal*, i.e., size independent, but dependent on the adopted model, dimensionality, symmetry, and even boundary conditions of the system. $w(T)$ has been studied for systems in two and more dimensions with a large number of attached single-channel leads.[15–26] In fact, concerning the conductance of one-dimensional (1D) systems and its statistical distribution, the regime of small number of leads has been left almost unexplored.[26–29]

In the present work we study numerically several statistical properties of the scattering matrix and the electronic transport across disordered systems in one and three dimensions described by the power-law banded random matrix (PBRM) model at criticality and the three-dimensional (3D) Anderson model at the MIT, respectively. We stress that we concentrate on the case of a small number of attached leads each of them supporting one open channel.

The organization of this paper is as follows. In the next section we define the PBRM model, the 3D Anderson model (3DAM), as well as the scattering setup. We also define the scattering quantities under investigation and provide the corresponding analytical predictions from random scattering-matrix theory (RMT) for systems with time-reversal symmetry. These analytical results will be used as a reference along the paper. In Sec. II we analyze the average-scattering matrix elements, the conductance probability distribution, the variance of the conductance, and the shot noise power for the PBRM model as a function of its effective bandwidth b. In Sec. III we compare the results of the PBRM model at criticality with the scattering and transport properties of the 3D Anderson model. Finally, Sec. IV is left for conclusions.

A. PBRM and the 3D Anderson models

As we have mentioned above, in the present study we adopt two models, namely, the PBRM model at criticality and the 3D Anderson model at the MIT. The PBRM model[4,30] describes 1D samples of length L with random long-range hopping. This model is represented by $N \times N$ ($N = L$) real symmetric matrices whose elements are statistically independent random variables drawn from a normal distribution with zero mean, $\langle H_{ij} \rangle = 0$, and a variance decaying as a power law $\langle |H_{ij}|^2 \rangle \sim (b/|i-j|)^{2\alpha}$, where b and α are parameters. There are two prescriptions for the variance of the PBRM model: the so-called nonperiodic,

$$\langle |H_{ij}|^2 \rangle = \frac{1}{2} \frac{1 + \delta_{ij}}{1 + (|i-j|/b)^{2\alpha}}, \tag{1}$$

 ©2010 The American Physical Society

where the 1D sample is in a *line* geometry; and the periodic,

$$\langle |H_{ij}|^2 \rangle = \frac{1}{2}\frac{1+\delta_{ij}}{1+[\sin(\pi|i-j|/L)/(\pi b/L)]^{2\alpha}}, \quad (2)$$

where the sample is in a *ring* geometry. Field-theoretical considerations[4,30,31] and detailed numerical investigations[4,32,33] have verified that the PBRM model undergoes a transition at $\alpha=1$ from localized states for $\alpha>1$ to delocalized states for $\alpha<1$. This transition shows all the key features of the Anderson MIT, including multifractality of eigenfunctions and nontrivial spectral statistics at the critical point. Thus the PBRM model possesses a line of critical points $b \in (0,\infty)$. We set $\alpha=1$ in our study, i.e., we work with the PBRM model at criticality.

The 3D Anderson model with diagonal disorder is described by the tight-binding Hamiltonian (TBH)

$$H = \sum_{\mathbf{n}} |\mathbf{n}\rangle W_{\mathbf{n}} \langle \mathbf{n}| + \sum_{(\mathbf{n},\mathbf{m})} |\mathbf{n}\rangle\langle \mathbf{m}|, \quad (3)$$

where $\mathbf{n} \equiv (n_x, n_y, n_z)$ labels all the $N=L^3$ sites of a cubic lattice with linear size L while the second sum is taken over all nearest-neighbor pairs $(\mathbf{n},\mathbf{m})$ on the lattice. The on-site potentials $W_{\mathbf{n}}$ for $1 \le n_x, n_y, n_z \le L$ are independent random variables. When $W_{\mathbf{n}}$ are Gaussian distributed, with zero mean and variance $W^2/12$, the MIT at energy $E \simeq 0$ occurs for $W = W_c \simeq 21.3$. See Refs. 17, 34, and 35. Then, for $W < W_c$ ($W > W_c$) the system is in the metallic (insulating) regime. We set $W=W_c$ in our study.

We open the isolated samples, defined above by the PBRM model and the 3D Anderson model, by attaching $2M$ semi-infinite single channel leads. Each lead is described by the 1D semi-infinite TBH

$$H_{\text{lead}} = \sum_{n=1}^{-\infty} (|n\rangle\langle n+1| + |n+1\rangle\langle n|). \quad (4)$$

Using standard methods[36] one can write the scattering matrix (S matrix) in the form[11,12]

$$S(E) = \begin{pmatrix} r & t' \\ t & r' \end{pmatrix} = 1 - 2i \sin(k) \mathcal{W}^T (E - \mathcal{H}_{\text{eff}})^{-1} \mathcal{W}, \quad (5)$$

where 1 is the $2M \times 2M$ unit matrix, $k=\arccos(E/2)$ is the wave vector supported in the leads, and $\mathcal{H}_{\text{eff}}$ is an effective non-Hermitian Hamiltonian given by

$$\mathcal{H}_{\text{eff}} = H - e^{ik} \mathcal{W}\mathcal{W}^T. \quad (6)$$

Here, $\mathcal{W}$ is an $N \times 2M$ matrix that specifies the positions of the attached leads to the sample. Its elements are equal to zero or ϵ, where ϵ is the coupling strength. Moreover, assuming that the wave vector k does not change significantly in the center of the band, we set $E=0$ and neglect the energy dependence of $\mathcal{H}_{\text{eff}}$ and S.

B. RMT predictions for the circular orthogonal ensemble

Notice from Eqs. (1) and (2) that in the limit $b \to \infty$ the PBRM model reproduces the Gaussian orthogonal ensemble. Therefore, in that limit we expect the statistics of the scattering matrix, Eq. (5), to be determined by the circular orthogonal ensemble (COE) which is the appropriate ensemble for systems with time reversal symmetry. Thus, below, we provide the statistical results for the average S matrix and the transport quantities to be analyzed in the following sections, assuming the orthogonal symmetry. In all cases, we also assume the absence of direct processes, i.e., $\langle S \rangle = 0$.

We start with the average of the S-matrix elements. It is known that

$$\langle |S_{aa'}|^2 \rangle_{\text{COE}} = \frac{1+\delta_{aa'}}{2M+1}, \quad (7)$$

where $\langle \cdot \rangle$ means ensemble average over the COE.

Within a scattering approach to the electronic transport, once the scattering matrix is known one can compute the dimensionless conductance $T=\text{Tr}(tt^\dagger)$ and its distribution $w(T)$. For $M=1$, i.e., considering two single-channel leads attached to the sample, $w(T)$ is given by

$$w(T)_{\text{COE}} = \frac{1}{2\sqrt{T}} \quad (8)$$

while for $M=2$,

$$w(T)_{\text{COE}} = \begin{cases} \frac{3}{2}T, & 0 < T < 1 \\ \frac{3}{2}(T - 2\sqrt{T-1}), & 1 < T < 2 \end{cases}. \quad (9)$$

For arbitrary M, the predictions for the average value of T and its variance are

$$\langle T \rangle_{\text{COE}} = \frac{M}{2} - \frac{M}{2(2M+1)} \quad (10)$$

and

$$\text{var}(T)_{\text{COE}} = \frac{M(M+1)^2}{(2M+1)^2(2M+3)}, \quad (11)$$

respectively. For the derivation of the expressions above see, for example, Ref. 37. Another transport quantity of interest is the shot noise power $P=\langle \text{Tr}(tt^\dagger - tt^\dagger tt^\dagger) \rangle$, which as a function of M reads[38–40]

$$P_{\text{COE}} = \frac{M(M+1)^2}{2(2M+1)(2M+3)}. \quad (12)$$

In the following sections we focus on $\langle |S_{aa'}|^2 \rangle$, $\langle T \rangle$, $\text{var}(T)$, and P for the PBRM model and the 3D Anderson model, both at the MIT. In all cases we set the coupling strength ϵ such that $\langle S \rangle \approx 0$ in order to compare our results, in the proper limits, with the RMT predictions introduced above.

II. PBRM MODEL

We attach the $2M$ leads to the first $2M$ sites of the 1D sample described by the PBRM model. That is, in the nonperiodic version of the PBRM model, Eq. (1), we attach the

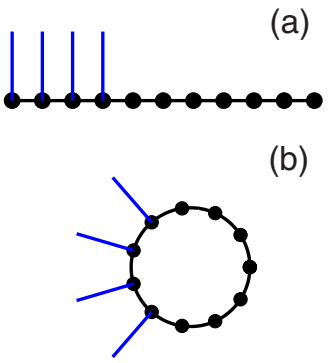

FIG. 1. (Color online) Scattering setup. $2M$ leads, shown as blue (gray) lines, are attached to $2M$ sites (black dots) of a 1D sample described by the (a) nonperiodic and (b) periodic versions of the PBRM model. The case $M=2$ with $L=11$ is shown as example.

leads at the *boundary* of the system. See Fig. 1(a). While in the periodic version, Eq. (2), we attach them to the *bulk*. See Fig. 1(b). In the latter case, finite size effects are considerably reduced. However, the quantities we analyze below are L independent once L is much larger than the number of attached leads for both versions of the PBRM model.

We point out that our setup is significantly different from the one used in Refs. 28 and 29, where the conductance has also been studied using the PBRM model. There, for example, the leads in the $M=1$ case are attached to sites which are separated a distance of $L/2$ and L in the periodic and nonperiodic versions of the PBRM model, respectively. In such situation the scattering quantities are strongly L dependent.

A. Average-scattering matrix elements

First we consider the case $M=1$, where the S matrix is a 2×2 matrix. In Fig. 2(a) we plot the ensemble average of the elements $|S_{11}|^2$ and $|S_{12}|^2$ as a function of the bandwidth parameter b, $\langle|S_{11}|^2\rangle_b$, and $\langle|S_{12}|^2\rangle_b$, for the periodic and the nonperiodic PBRM model. We concentrate on these two matrix elements since the other two elements give no additional information: $\langle|S_{22}|^2\rangle_b=\langle|S_{11}|^2\rangle_b$ and $\langle|S_{21}|^2\rangle_b=\langle|S_{12}|^2\rangle_b$. Notice a strong b dependence of the average S-matrix elements driving them from a localizedlike regime $[\langle|S_{11}|^2\rangle\approx 1$ and $\langle|S_{12}|^2\rangle\approx 0$; i.e., the average conductance is close to zero] for $b\ll 1$, to a delocalizedlike or ballisticlike regime $[\langle|S_{11}|^2\rangle \approx 2/3$ and $\langle|S_{12}|^2\rangle\approx 1/3$; i.e., RMT results are already recovered] for $b\geq 4$.

Moreover, we have found that $\langle|S_{11}|^2\rangle$ and $\langle|S_{12}|^2\rangle$, as a function of the bandwidth b, are well described by

$$\langle|S_{11}|^2\rangle_b = 1-\langle|S_{12}|^2\rangle_b, \tag{13}$$

$$\langle|S_{12}|^2\rangle_b = \frac{1}{3}\left[\frac{1}{1+(\delta b)^{-2}}\right], \tag{14}$$

where δ is a fitting parameter. Equation (13) is a consequence of the unitarity of the scattering matrix, $SS^\dagger=1$ while the factor 1/3 in Eq. (14) comes from Eq. (7) with $M=1$. In Fig. 2(a) we plot Eqs. (13) and (14) (dashed lines) and compare them with the corresponding results from the PBRM model (symbols) in the periodic and nonperiodic setups. In the same figure Eq. (7) is also plotted (dotted-dashed lines).

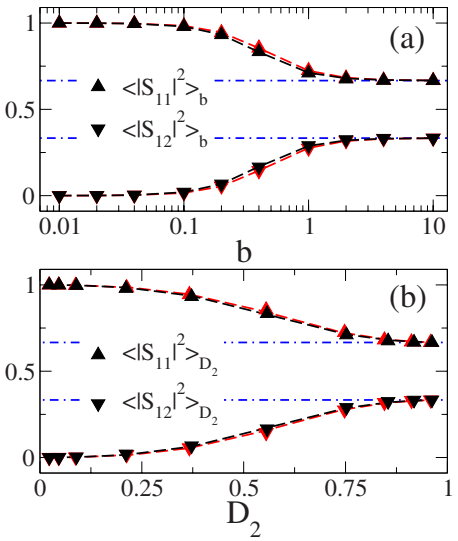

FIG. 2. (Color online) Black [red (gray)] symbols: average S-matrix elements $\langle|S_{11}|^2\rangle$ and $\langle|S_{12}|^2\rangle$ for the periodic [nonperiodic] PBRM model at criticality as a function of (a) b and (b) D_2 for $M=1$. The blue (gray) dotted-dashed lines correspond to 2/3 and 1/3; the RMT prediction for $\langle|S_{11}|^2\rangle$ and $\langle|S_{12}|^2\rangle$, respectively, given by Eq. (7). The black [red (gray)] dashed lines in (a) are Eqs. (13) and (14) with $\delta\approx 2.5$ [$\delta\approx 2.2$]. The black [red (gray)] dashed lines in (b) are Eqs. (18) and (19) with $\delta\approx 2.5$ [$\delta\approx 2.2$]. Error bars are not shown since they are much smaller than symbol size.

On the other hand, it is well known that in systems at the disorder driven MIT both the energy spectra and the eigenstates exhibit multifractal characteristics.[4] The PBRM model is characterized by the effective bandwidth b that drives the system from strong ($b\to 0$) to weak ($b\to\infty$) multifractality. Multifractality can be quantified by the generalized dimensions D_q which describe the fluctuations of the eigenfunctions. The multifractal dimensions D_q of the σth eigenfunction Ψ^σ (given as a linear combination of the basis states in a system with linear size L, $\Psi^\sigma=\Sigma_{l=1}^{L} C_l^\sigma \phi_l$) are defined through the so-called inverse participation numbers, $\mathcal{I}_q=\Sigma_{l=1}^{L}|C_l^\sigma|^{2q}$, by the scaling[4,33,41]

$$(\mathcal{I}_q)^{\text{typ}} \propto L^{-(q-1)D_q}, \tag{15}$$

where $(\mathcal{I}_q)^{\text{typ}}=\exp\langle \ln \mathcal{I}_q\rangle$ is the typical value of $\mathcal{I}_q$. However, among all dimensions, the correlation dimension D_2 plays a prominent role.[42] As b transits from zero to infinity, D_2 takes values from zero to one.

Using numerical diagonalization of matrices with sizes $L=128$, 256, 512, and 1024, we extracted D_2 by the use of Eq. (15). For each system size L, we used a number of disorder realizations in order to have at least 10^5 data for its analysis. For each disorder realization we used 25% of the states at the center of the spectral band (where the density of states is almost constant) in order to avoid boundary effects. We found good agreement between the numerically obtained D_2 and the analytical estimation[4,41]

$$D_2 = \begin{cases} 2b, & b \ll 1 \\ 1 - (\pi b)^{-1}, & b \gg 1 \end{cases}. \quad (16)$$

Moreover, in Ref. 43 the following phenomenological analytical expression for D_2 as a function of b was proposed:

$$D_2(b) = \frac{1}{1 + (\gamma b)^{-1}}, \quad (17)$$

where γ is a fitting parameter. See also Ref. 14. Equation (17) describes well our numerical results for D_2 with $\gamma = 2.94$ and $\gamma = 2.88$ for the periodic and nonperiodic versions of the PBRM model, respectively.

Then, by substituting Eq. (17) into Eqs. (13) and (14) we obtain the following expressions for the averages of $|S_{11}|^2$ and $|S_{12}|^2$ as a function of D_2:

$$\langle |S_{11}|^2 \rangle_{D_2} = 1 - \langle |S_{12}|^2 \rangle_{D_2}, \quad (18)$$

$$\langle |S_{12}|^2 \rangle_{D_2} = \frac{1}{3} \frac{1}{1 + (\gamma/\delta)^2 (D_2^{-1} - 1)^2}. \quad (19)$$

In Fig. 2(b) we compare Eqs. (18) and (19) (dashed lines) with the ensemble-average numerical results at different values of D_2. The agreement is excellent. In addition, it is interesting to note that

$$\langle |S_{12}|^2 \rangle_{D_2} \propto \begin{cases} D_2^2, & D_2 \to 0 \\ 1 - (\gamma/\delta)^2 (D_2^{-1} - 1)^2, & D_2 \to 1 \end{cases}, \quad (20)$$

which might be relevant for systems at the MIT where D_2 can be tuned.

Finally we want to remark that concerning $\langle |S_{aa'}|^2 \rangle$ for the PBRM model, the RMT limit, expected for $b \to \infty$, is already recovered for $b \geq 4$. See Fig. 2(a).

B. Conductance probability distribution

Now we turn to the conductance statistics. For $b \ll 1$ the conductance distribution $w(T)$ is highly concentrated close to $T = 0$. So it is more convenient to analyze the distribution of the transmission logarithm, $\rho(\ln T)$, instead. Then, in Fig. 3(a) we show $\rho(\ln T)$ for several values of $b < 1$ in the case $M = 1$, for the periodic and nonperiodic versions of the PBRM model. Notice that the distribution functions $\rho(\ln T)$ do not change their shape by increasing b, mainly for $b \ll 1$, thus being scale invariant. In fact, $\langle \ln T \rangle$ for $b < 1$ clearly displays a linear behavior when plotted as a function of $\ln b$ as shown in Fig. 3(b). Then, all distributions functions $\rho(\ln T)$ fall one on top of the other when shifting them along the x axis by the typical value of T,

$$T_{\text{typ}} = \exp\langle \ln T \rangle \quad (21)$$

as shown in Fig. 3(c).

Note that for $T < T_{\text{typ}}$, $\rho(\ln T)$ is proportional to $(T/T_{\text{typ}})^{1/2}$, see Figs. 3(a) and 3(c). Moreover, we found that such behavior extends from small to large values of b, $b \gg 1$. Also, notice that the behavior $\rho(\ln T) \propto T^{1/2}$ for small T coincides with the RMT prediction $w(T)_{\text{COE}} \propto T^{-1/2}$, see Eq. (8) since the change of variable $T \to \ln T$ leads to $\rho(\ln T) = T w_{\text{COE}}(T)$.

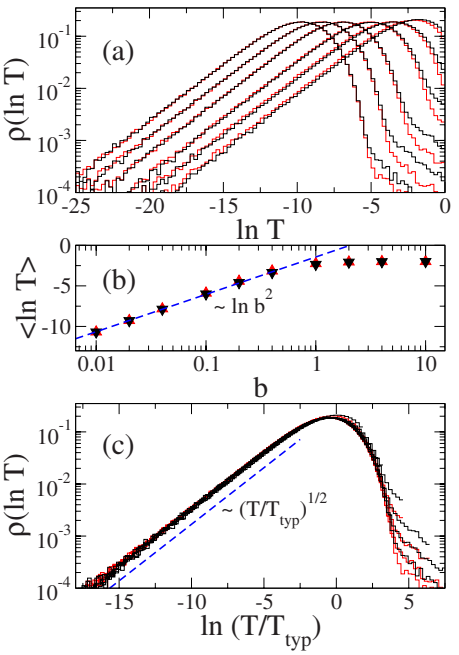

FIG. 3. (Color online) (a) Black [red (gray)] curves: probability distribution $\rho(\ln T)$ for the periodic [nonperiodic] PBRM model at criticality for several values of $b < 1$ ($b = 0.01$, 0.02, 0.04, 0.1, 0.2, and 0.4 from left to right) in the case $M = 1$. (b) Black [red (gray)] symbols: $\langle \ln T \rangle$ as a function of b for the periodic [nonperiodic] PBRM model. The blue (gray) dashed line is the best fit of the data to the logarithmic function $A + \ln b^2$ with $A \approx -1.44$. (c) $\rho(\ln T)$ for $b < 1$ scaled to $T_{\text{typ}} = \exp\langle \ln T \rangle \sim b^2$. The blue (gray) dashed line proportional to $(T/T_{\text{typ}})^{1/2}$ is plotted to guide the eyes.

In Fig. 4 we show $w(T)$ for large b ($b \geq 0.4$). In the limit $b \to \infty$, $w(T)$ is expected to approach the RMT prediction of Eq. (8). However, once $b \geq 4$, $w(T)$ is already well described by $w(T)_{\text{COE}}$.

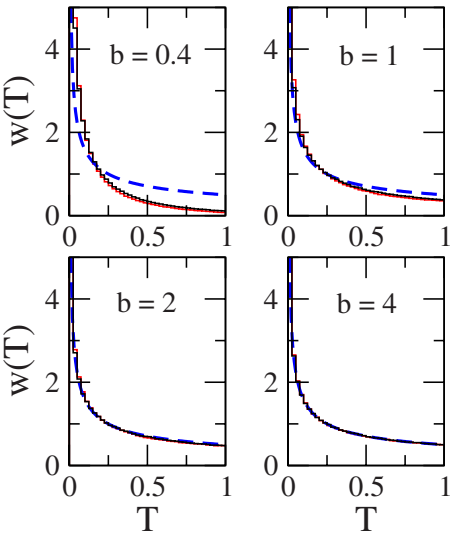

FIG. 4. (Color online) Black [red (gray)] curves: conductance probability distribution $w(T)$ for the periodic [nonperiodic] PBRM model at criticality for some *large* values of b in the case $M = 1$. Blue (gray) dashed lines are $w(T)_{\text{COE}}$; the RMT prediction for $w(T)$ given by Eq. (8).

TABLE I. $\langle \ln T \rangle$ for the periodic PBRM model at criticality for some values of b and L in the case $M=1$.

L	$b=0.1$	$b=1$	$b=10$
50	-5.887 ± 0.002	-2.249 ± 0.002	-2.001 ± 0.002
100	-5.886 ± 0.002	-2.247 ± 0.002	-1.999 ± 0.002
200	-5.875 ± 0.002	-2.245 ± 0.002	-1.999 ± 0.002
400	-5.875 ± 0.002	-2.244 ± 0.002	-2.002 ± 0.002
800	-5.869 ± 0.002	-2.228 ± 0.002	-1.989 ± 0.002

We want to stress that our results do not depend on the system size L, as can be seen in Table I where we report $\langle \ln T \rangle$ for the periodic PBRM model at criticality for some values of b and L in the case $M=1$. In fact, $\langle \ln T \rangle$ does not depend on L out of criticality ($\alpha>1$ and $\alpha<1$) either. This makes an important difference with respect to the setup where the leads are attached to opposite sides of the sample where $\langle \ln T \rangle$ increases (decreases) as a function of L for $\alpha<1$ ($\alpha>1$ and $\alpha=1$).

Now, in Figs. 5 and 6 we explore $w(T)$ in the case $M=2$. As well as in the case $M=1$, studied above, here: (i) for small b, $\rho(\ln T)$ is scale invariant with T_{typ} as scaling factor, see Fig. 5; (ii) for $b \geq 4$, $w(T)$ is well described by Eq. (9), the corresponding RMT prediction, see Fig. 6. However, although $\rho(\ln T)$ for small b and $w(T)$ for large b are practically the same for the periodic and nonperiodic versions of the PBRM model, they show differences for intermediate values, $0.1<b<4$, as can be seen in Fig. 5(a) and the upper panels of Fig. 6.

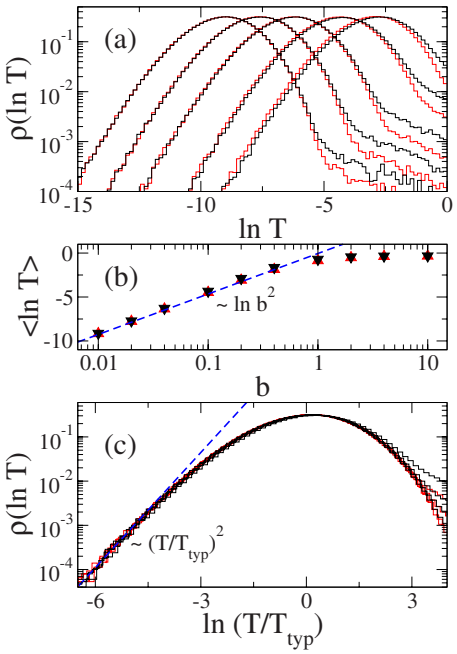

FIG. 5. (Color online) (a) Black [red (gray)] curves: probability distribution $\rho(\ln T)$ for the periodic [nonperiodic] PBRM model at criticality for several values of $b<1$ ($b=0.01$, 0.02, 0.04, 0.1, and 0.2 from left to right) in the case $M=2$. (b) Black [red (gray)] symbols: $\langle \ln T \rangle$ as a function of b for the periodic [nonperiodic] PBRM model. The blue (gray) dashed line is the best fit of the data to the logarithmic function $A+\ln b^2$ with $A \approx -0.057$. (c) $\rho(\ln T)$ for $b<1$ scaled to $T_{\text{typ}}=\exp\langle \ln T \rangle \sim b^2$. The blue (gray) dashed line proportional to $(T/T_{\text{typ}})^2$ is plotted to guide the eyes.

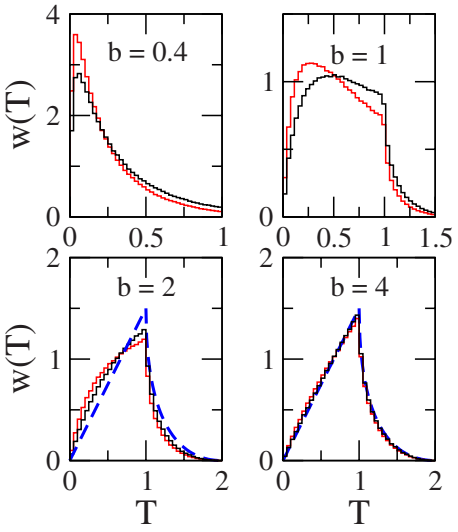

FIG. 6. (Color online) Black [red (gray)] curves: conductance probability distribution $w(T)$ for the periodic [nonperiodic] PBRM model at criticality for some *large* values of b in the case $M=2$. Blue (gray) dashed lines are $w(T)_{\text{COE}}$; the RMT prediction for $w(T)$ given by Eq. (9).

We point out that for small T, $T \ll T_{\text{typ}}$, $\rho(\ln T)$ is proportional to $(T/T_{\text{typ}})^2$, as shown in Fig. 5(c). This behavior is universal for the PBRM model with $M=2$; i.e., it is b independent and valid for the periodic and nonperiodic versions of the model. Again, as for the $M=1$ case, here for $M=2$, the dependence $\rho(\ln T) \propto T^2$ in the limit $b \to \infty$ is consistent with the RMT prediction $w(T)_{\text{COE}} \propto T$ for $T<1$; see Eq. (9).

From the results above and since[37]

$$w(T)_{\text{COE}} \propto T^{M^2/2-1}, \tag{22}$$

in the region $0<T<1$, we conclude that for the PBRM model

$$\rho(\ln T) \propto T^{M^2/2}, \tag{23}$$

for $T \ll T_{\text{typ}}$. We argue that the behavior dictated by Eq. (23) can be interpreted in the following way: Since small values of conductance $T \ll 1$ mean very strong reflection, the scattering process is almost direct, i.e., an incident electron is scattered out the system mainly by the interaction with the sites at which the leads are attached. Then the electron does not explore the complete sample, not even part of it, and as a consequence it does not realize that the sample is at criticality. That is, for $T \ll 1$, the incident electron does not distinguish between a critical system and a random system represented by a full random matrix if the number of attached leads $2M$ is not much larger than b; i.e., when the leads are attached to sites interconnected by Hamiltonian matrix elements located within the bandwidth of the matrix where all elements have almost the same variance: $\langle |H_{ij}|^2 \rangle \approx 1/2$. So, we can use Eq. (22) and as a consequence Eq. (23) too. In fact, we have verified that Eq. (23) is valid up to $M=2$ for

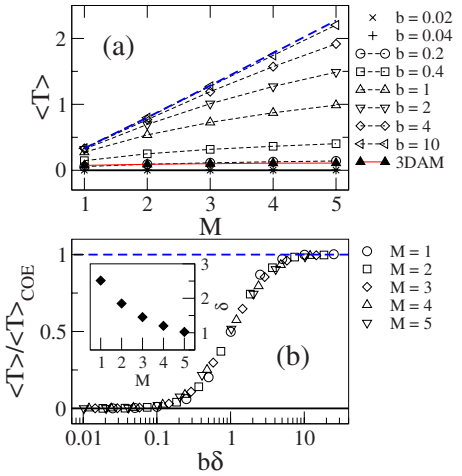

FIG. 7. (Color online) (a) Average conductance $\langle T\rangle$ as a function of M for the nonperiodic PBRM model at criticality for several values of b. $\langle T\rangle$ for the 3D Anderson model at criticality (3DAM) is also shown. (b) $\langle T\rangle/\langle T\rangle_{\mathrm{COE}}$ as a function of $b\delta$ for the periodic PBRM model at criticality for $M\in[1,5]$. Insert: δ versus M. δ is obtained from the fitting of Eq. (24) to the $\langle T\rangle$ vs b data. Thick full lines correspond to $\langle T\rangle=0$. Blue (gray) dashed lines are (a) the RMT prediction for $\langle T\rangle$ given by Eq. (10); and (b) one.

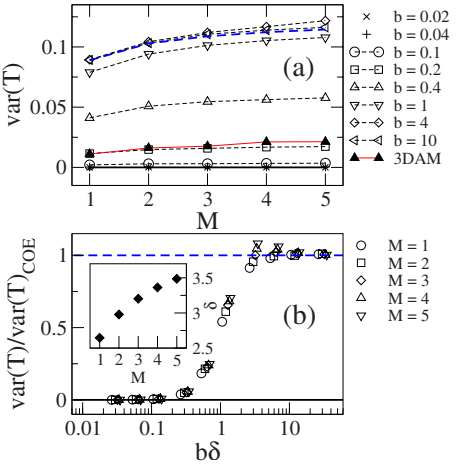

FIG. 8. (Color online) (a) Variance of T as a function of M for the nonperiodic PBRM model at criticality for several values of b. var(T) for the 3DAM at criticality is also shown. (b) var(T)/var(T)$_{\mathrm{COE}}$ as a function of $b\delta$ for the periodic PBRM model at criticality for $M\in[1,5]$. Insert: δ versus M. δ is obtained from the fitting of Eq. (24) to the var(T) vs b data. Thick full lines correspond to var(T)=0. Blue (gray) dashed lines are (a) the RMT prediction for var(T) given by Eq. (11); and (b) one.

$b\leq 1$ while for $b=10$ it describes perfectly the left tail of $\rho(\ln T)$ for all the values of M used in this work (up to $M=5$). Our result, given by Eq. (23), is the generalization of the result shown in Ref. 28, where the behavior $\rho(\ln T)\propto T^{1/2}$ was reported for the PBRM model in the localized ($\alpha>1$) and delocalized regimes ($\alpha<1$) for $M=1$.

C. Mean and variance of the conductance and the shot noise power

We now increase further the number of attached leads.[44] In Figs. 7(a), 8(a), and 9(a) we plot the average conductance $\langle T\rangle$, the variance of the conductance var(T), and the shot noise power P for the nonperiodic version of the PBRM model for several values of b with $M\in[1,5]$.[45] It is clear from these three plots that changing b from small ($b\ll 1$) to large ($b>1$) values produces a transition from localized to delocalizedlike behavior in the scattering properties of the PBRM model. That is, (i) for $b<0.1$, $\langle T\rangle\approx 0$, var($T$)$\approx 0$, and $P\approx 0$; and (ii) for $b\geq 10$, $\langle T\rangle$, var(T), and P are well described by the corresponding RMT predictions given by Eqs. (10)–(12), respectively. Similar plots are obtained (not shown here) for the periodic PBRM model.

Moreover, we have observed that $\langle T\rangle$, var(T), and P behave (for all M) as $\langle|S_{12}|^2\rangle_b$ does. See Eq. (14). Thus, we can write

$$X(b)=X_{\mathrm{COE}}\left[\frac{1}{1+(\delta b)^{-2}}\right], \tag{24}$$

where X represents $\langle T\rangle$, var(T), or P and δ is a fitting parameter. Then, in Figs. 7(b), 8(b), and 9(b) we plot $\langle T\rangle$, var(T), and P normalized to their respective COE average values, now for the periodic PBRM model as a function of $b\delta$ for $M\in[1,5]$. Also, similar plots are obtained (not shown here) for the nonperiodic PBRM model.

III. 3D ANDERSON MODEL

Since the most prominent realization of systems that undergo a MIT is the 3D Anderson model, it is of relevance to analyze its scattering and transport properties taking as a reference the results shown in the previous section for the PBRM model.

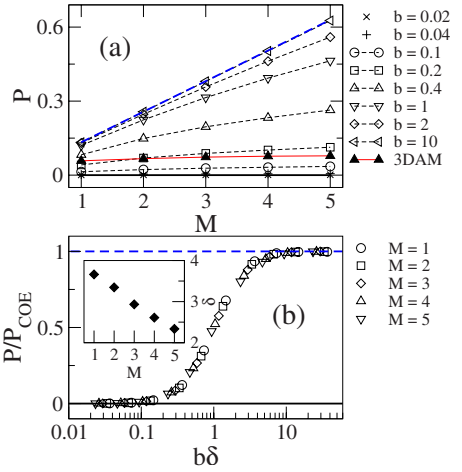

FIG. 9. (Color online) (a) Shot noise power P as a function of M for the nonperiodic PBRM model at criticality for several values of b. P for the 3DAM at criticality is also shown. (b) P/P_{COE} as a function of $b\delta$ for the periodic PBRM model at criticality for $M\in[1,5]$. Insert: δ versus M. δ is obtained from the fitting of Eq. (24) to the P vs b data. Thick full lines correspond to $P=0$. Blue (gray) dashed lines are (a) the RMT prediction for P given by Eq. (12); and (b) one.

TABLE II. Average S-matrix elements $\langle|S_{11}|^2\rangle$ and $\langle|S_{12}|^2\rangle$ for the 3D Anderson model at criticality for some values of L in the case $M=1$.

L	$\langle\|S_{11}\|^2\rangle$	$\langle\|S_{12}\|^2\rangle$
6	0.9256 ± 0.0001	0.0743 ± 0.0001
8	0.9254 ± 0.0003	0.0745 ± 0.0003
10	0.926 ± 0.001	0.073 ± 0.001

We attach the $2M$ leads to $2M$ sites at one of the edges of the cubic lattice described by the 3D Anderson model. In this way we make a *line contact* as we did in the case of the PBRM model. So, we can compare the scattering properties of both models. We use Gaussian distributed on-site potentials and system sizes from $L=6$ to 10 (we have verified that our results do not change by increasing L further) with 10^6 to 10^4 disorder realizations.

We start our analysis by looking at the average-scattering matrix elements for $M=1$. For the 3D Anderson model at criticality we found $\langle|S_{11}|^2\rangle \approx 0.926$ and $\langle|S_{12}|^2\rangle \approx 0.074$, see Table II, which are close to those of the nonperiodic PBRM model with $b=0.24$.

In Fig. 10 we show conductance probability distributions $\rho(\ln T)$ for the 3D Anderson model at criticality in the cases $M=1$ and $M=2$. We found $\langle \ln T\rangle \approx -3.47$ and -3.06 for $M=1$ and $M=2$, respectively. See Table III. These values of $\langle \ln T\rangle$ for the 3D Anderson model are close to those of the PBRM model with $b=0.36$ and $b=0.22$, respectively. Notice also that, as well as for the PBRM model, for the 3D Anderson model $\rho(\ln T)$ in the region of $T \ll T_{\text{typ}}$ is proportional to $(T/T_{\text{typ}})^{1/2}$ and $(T/T_{\text{typ}})^2$ for $M=1$ and $M=2$, respectively (dashed lines in Fig. 10).

Additionally, in Fig. 11 we plot $w(T)$ for the 3D Anderson model in the cases $M=1$ and $M=2$. In the same figure we have also plotted (dashed lines) the conductance distributions from the PBRM model with $b=0.2$. We can see that the conductance distributions of both models are similar at this bandwidth value.

We also compute $\langle T\rangle$, var(T), and P for the 3D Anderson model and plot them in Figs. 7(a), 8(a), and 9(a), respectively (red curves labeled as 3DAM). We observe that for the 3D Anderson model $\langle T\rangle$, var(T), and P behave as the corresponding quantities for the PBRM model with b close to 0.2.

We want to stress that our results for the 3D Anderson model at criticality do not seem to depend on the on-site potential distribution. Here we used Gaussian distributed potentials. However, we observe practically the same results by the use of box distributed on-site potentials (not shown here).

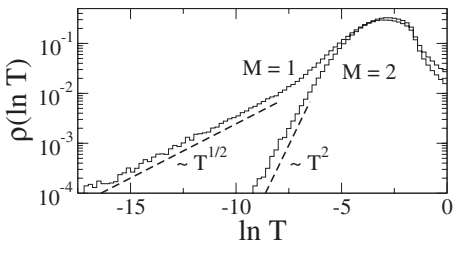

FIG. 10. Probability distribution $\rho(\ln T)$ for the 3D Anderson model at criticality in the cases $M=1$ and $M=2$. Dashed lines with slopes $T^{1/2}$ and T^2 are plotted to guide the eyes.

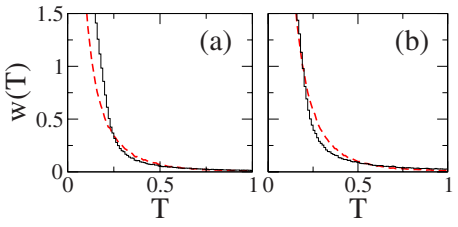

FIG. 11. (Color online) Conductance probability distribution $w(T)$ for the 3D Anderson model at criticality in the cases (a) $M=1$ and (b) $M=2$. The red (gray) dashed line corresponds to $w(T)$ for the nonperiodic PBRM model with $b=0.2$.

IV. CONCLUSIONS

We study the scattering and transport properties of the PBRM model and of the three-dimensional (3D) Anderson model, both at criticality. We observed a smooth crossover from localized to delocalizedlike (ballisticlike) behavior in the scattering properties of the PBRM model by varying b from small ($b \ll 1$) to large ($b > 1$) values. For this crossover region we proposed heuristic analytical expressions for $\langle|S_{aa'}|^2\rangle_b$ and $\langle|S_{aa'}|^2\rangle_{D_2}$. For small b, we have shown that $\rho(\ln T)$ is scale invariant with the typical value of T, T_{typ}, as scaling factor. We realized that RMT results, expected in the limit $b \to \infty$, are already recovered for relatively small values of the bandwidth: $b \geq 10$. However, this fact is closely related to the small number of attached leads we used in this work: the larger the number of leads the larger the value of b needed to approach RMT behavior.

Our conclusions are valid for leads attached to the bulk of the system as well as for leads attached at the boundary. In this work we assumed that time-reversal symmetry ($\beta=1$) is present in our disordered systems. Moreover, the case of broken time-reversal symmetry ($\beta=2$) has been preliminarily studied in Ref. 46 where similar conclusions to this work were made.

We have also shown that the scattering properties of the 3D Anderson model are similar to those for the PBRM model with $b \in [0.2, 0.4]$. This result is in agreement with previous studies[32] were it was shown that several critical quantities related to the spectrum and eigenstates of the PBRM model with $b=0.3$ are practically the same as for the 3D Anderson model. This makes the PBRM model an excellent candidate to explore the properties of the 3D Anderson model at criticality at a low-computational cost.

TABLE III. $\langle \ln T\rangle$ for the 3D Anderson model at criticality for some values of L in the cases $M=1$ and $M=2$.

L	$\langle \ln T\rangle(M=1)$	$\langle \ln T\rangle(M=2)$
6	-3.471 ± 0.001	-3.060 ± 0.001
8	-3.483 ± 0.005	-3.058 ± 0.003
10	-3.450 ± 0.016	-3.078 ± 0.012

We want to stress that for both models at criticality, the PBRM model and the 3D Anderson model, we found the universal behavior $\rho(\ln T) \propto T^{M^2/2}$ for $T \ll 1$, that we tested here for $M=1$ and $M=2$. Moreover by the use of the PBRM model with $\beta=2$ (not shown here) we have already verified that the more general expression $\rho(\ln T) \propto T^{\beta M^2/2}$, derived from[37] $w(T) \propto T^{\beta M^2/2-1}$ with $0<T<1$, holds.

We emphasize that, even though we used a scattering setup where the leads are attached perfectly to sites at one side of the sample, our conclusions are not restricted to this topology.[47]

Finally, we recall that we concentrate here on the case of a small number of single-channel attached leads (up to ten). The study of the scattering and transport properties of the PBRM and the 3D Anderson models in the regime of $M \gg 1$ will be the subject of a forthcoming contribution.[48]

ACKNOWLEDGMENTS

This work was partially supported by the Hungarian-Mexican Intergovernmental S & T Cooperation Program under Grants No. MX-16/2007 (NKTH) and No. I0110/127/08 (CONACyT). We also acknowledge support form CONACyT Mexico under Grant No. CB-2006-01-60879; the European Social Fund; the MICINN (Spain) under Project No. FIS 2009-16450 and through the Ramón y Cajal Program; the Alexander von Humboldt Foundation; and the Hungarian Research Fund (OTKA) under Grants No. K73361 and No. K75529.

[1] P. W. Anderson, Phys. Rev. **109**, 1492 (1958); B. Kramer and A. MacKinnon, Rep. Prog. Phys. **56**, 1469 (1993); E. Abrahams, P. W. Anderson, D. C. Licciardello, and T. V. Ramakrishnan, Phys. Rev. Lett. **42**, 673 (1979); L. P. Gorkov, A. I. Larkin, and D. E. Khmelnitskii, JETP Lett. **30**, 228 (1979).

[2] *Mesoscopic Quantum Physics*, Proceedings of the Les Houches Session LXI, edited by E. Akkermans, G. Montambaux, J.-L. Pichard, and J. Zinn-Justin (North-Holland, Amsterdam, 1995).

[3] B. L. Altshuler, V. E. Kravtsov, and I. V. Lerner, in *Mesoscopic Phenomena in Solids*, edited by B. L. Altshuler, P. A. Lee, and R. A. Webb (North-Holland, Amsterdam, 1991).

[4] F. Evers and A. D. Mirlin, Rev. Mod. Phys. **80**, 1355 (2008).

[5] J. A. Méndez-Bermúdez and T. Kottos, Phys. Rev. B **72**, 064108 (2005).

[6] A. Ossipov and Y. V. Fyodorov, Phys. Rev. B **71**, 125133 (2005).

[7] A. D. Mirlin, Y. V. Fyodorov, A. Mildenberger, and F. Evers, Phys. Rev. Lett. **97**, 046803 (2006).

[8] A. Ossipov, T. Kottos, and T. Geisel, Europhys. Lett. **62**, 719 (2003).

[9] Y. V. Fyodorov, JETP Lett. **78**, 250 (2003).

[10] C. Texier and A. Comtet, Phys. Rev. Lett. **82**, 4220 (1999); A. Ossipov, T. Kottos, and T. Geisel, Phys. Rev. B **61**, R11411 (2000).

[11] T. Kottos and M. Weiss, Phys. Rev. Lett. **89**, 056401 (2002).

[12] F. Steinbach, A. Ossipov, T. Kottos, and T. Geisel, Phys. Rev. Lett. **85**, 4426 (2000).

[13] M. Weiss, J. A. Méndez-Bermúdez, and T. Kottos, Phys. Rev. B **73**, 045103 (2006).

[14] J. A. Méndez-Bermúdez and I. Varga, Phys. Rev. B **74**, 125114 (2006).

[15] B. Shapiro, Phys. Rev. Lett. **65**, 1510 (1990).

[16] P. Markoš, Europhys. Lett. **26**, 431 (1994).

[17] P. Markoš, Phys. Rev. Lett. **83**, 588 (1999).

[18] K. Slevin and T. Ohtsuki, Phys. Rev. Lett. **78**, 4083 (1997).

[19] K. Slevin, T. Ohtsuki, and T. Kawarabayashi, Phys. Rev. Lett. **84**, 3915 (2000).

[20] K. Slevin, P. Markoš, and T. Ohtsuki, Phys. Rev. Lett. **86**, 3594 (2001).

[21] X. Wang, Q. Li, and C. M. K. Soukoulis, Phys. Rev. B **58**, 3576 (1998).

[22] M. Rühländer and C. M. Soukoulis, Physica B **296**, 32 (2001).

[23] M. Rühländer, P. Markoš, and C. M. Soukoulis, Phys. Rev. B **64**, 212202 (2001).

[24] I. Travěnec and P. Markoš, Phys. Rev. B **65**, 113109 (2002).

[25] L. Schweitzer and P. Markoš, Phys. Rev. Lett. **95**, 256805 (2005); P. Markoš and L. Schweitzer, J. Phys. A **39**, 3221 (2006).

[26] M. Janssen, M. Metzler, and M. R. Zirnbauer, Phys. Rev. B **59**, 15836 (1999).

[27] K. Senouci and N. Zekri, Phys. Rev. B **66**, 212201 (2002).

[28] C. Monthus and T. Garel, Phys. Rev. B **79**, 205120 (2009).

[29] C. Monthus and T. Garel, J. Stat. Mech.: Theory Exp. 2009, P07033.

[30] A. D. Mirlin, Y. V. Fyodorov, F.-M. Dittes, J. Quezada, and T. H. Seligman, Phys. Rev. E **54**, 3221 (1996).

[31] V. E. Kravtsov and K. A. Muttalib, Phys. Rev. Lett. **79**, 1913 (1997); V. E. Kravtsov and A. M. Tsvelik, Phys. Rev. B **62**, 9888 (2000).

[32] E. Cuevas, M. Ortuno, V. Gasparian, and A. Perez-Garrido, Phys. Rev. Lett. **88**, 016401 (2001).

[33] I. Varga, Phys. Rev. B **66**, 094201 (2002); I. Varga and D. Braun, *ibid.* **61**, R11859 (2000).

[34] A. Cohen, Y. Roth, and B. Shapiro, Phys. Rev. B **38**, 12125 (1988); C. M. Soukoulis, X. S. Wang, Q. M. Li, and M. M. Sigalas, Phys. Rev. Lett. **82**, 668 (1999); K. Slevin and T. Ohtsuki, *ibid.* **82**, 382 (1999).

[35] K. A. Muttalib and P. Wölfle, Phys. Rev. Lett. **83**, 3013 (1999).

[36] C. Mahaux and H. A. Weidenmüller, *Shell Model Approach in Nuclear Reactions* (North-Holland, Amsterdam, 1969); J. J. M. Verbaarschot, H. A. Weidenmüller, and M. R. Zirnbauer, Phys. Rep. **129**, 367 (1985); I. Rotter, Rep. Prog. Phys. **54**, 635 (1991).

[37] P. A. Mello and N. Kumar, *Quantum Transport in Mesoscopic Systems* (Oxford University Press, Oxford, 2004).

[38] E. N. Bulgakov, V. A. Gopar, P. A. Mello, and I. Rotter, Phys. Rev. B **73**, 155302 (2006).

[39] S. Heusler, S. Müller, P. Braun, and F. Haake, Phys. Rev. Lett. **96**, 066804 (2006); P. Braun, S. Heusler, S. Müller, and F. Haake, J. Phys. A **39**, L159 (2006).

[40] D. V. Savin and H.-J. Sommers, Phys. Rev. B **73**, 081307(R) (2006).
[41] F. Evers and A. D. Mirlin, Phys. Rev. Lett. **84**, 3690 (2000).
[42] H. G. E. Hentschel and I. Procaccia, Physica D **8**, 435 (1983); I. Varga and J. Pipek, J. Phys.: Condens. Matter **10**, 305 (1998).
[43] J. A. Méndez-Bermúdez, T. Kottos, and D. Cohen, Phys. Rev. E **73**, 036204 (2006).
[44] All quantities reported in Figs. 2–6 were obtained for $L=50$ using 10^6 ensemble realizations. In Sec. II C we used $L=200$ and 10^5 ensemble realizations. We have verified that in both cases our results are invariant by further increasing L. See also Table I.
[45] We recall that for $M=5$, ten single-channel leads are attached to the sample.
[46] A. Alcazar-López, J. A. Méndez-Bermúdez, and I. Varga, Ann. Phys. (Berlin) **18**, 896 (2009).
[47] J. A. Méndez-Bermúdez, V. A. Gopar, and I. Varga (unpublished).
[48] In Ref. 29 some properties of the transmission for the PBRM model were already studied for $M \gg 1$.